

Understanding Mid-Latitude Jet Variability and Change using Rossby Wave Chromatography: Methodology

DAVID J. LORENZ *

Center for Climatic Research, University of Wisconsin-Madison, Madison, WI

ABSTRACT

Rossby Wave Chromatography (RWC) is implemented in a linearized barotropic model as a tool to diagnose and understand the interaction between the mid-latitude jet and the eddies. Given the background zonal-mean flow and the space-time structure of the baroclinic wave activity source, RWC calculates the space-time structure of the upper tropospheric eddy momentum fluxes. Using the convergence of the vertical EP flux in the upper troposphere as the wave source, RWC reproduces the main features of a GCM's mean state and response to external forcing. When coupled to the zonal-mean zonal wind and a simple model of wave activity source phase speed changes RWC also simulates the temporal evolution of the GCM's internally generated zonal-mean zonal wind anomalies. Because the full space-time structure of the baroclinic wave activity source is decoupled from the background flow, RWC can be used to isolate and quantify the dynamical mechanisms responsible for 1) the poleward shift of the mid-latitude jet and 2) the feedbacks between the eddy momentum fluxes and the background flow in general.

1. Introduction

This is the first in a series of papers on understanding and quantifying the fundamental dynamical mechanisms responsible for the eddy momentum flux response to zonal-mean zonal wind anomalies. Since the effect of the eddies on the zonal-mean in the extratropics is well known, the above theory will help provide an explanation for the structure of mid-latitude jet variability and the response of the mid-latitude jet to external forcing. In this paper, we develop a model designed to cleanly separate dynamical mechanisms. The model is based on the idea that a theory for eddy fluxes can be usefully divided into two components: 1) a theory for the space-time structure of wave activity propagating into the upper troposphere from baroclinic instability and 2) a theory of the meridional propagation of the waves in the upper troposphere that determine the pattern of wave dissipation and the resulting mean flow deceleration (Held and Hoskins (1985); Held and Phillips (1987); Randel

and Held (1991)). In this paper, we focus on developing a quantitative model for part two of this eddy closure, which Held and Phillips (1987) gave the name Rossby Wave Chromatography (RWC). We also propose a simple model for the changes in the phase speed spectrum of the wave activity propagating into the upper troposphere from baroclinic instability.

The dynamical model for our implementation of RWC is the forced, linearized barotropic vorticity equation. Forced barotropic and shallow water models have been used before to understand zonal-mean zonal wind variability and change (Vallis et al. (2004); Chen et al. (2007); Barnes et al. (2010); Barnes and Hartmann (2011); Kidston and Vallis (2012)). Unlike these studies, which specify the forcing directly, we specify the baroclinic wave activity source and find the forcing that is consistent with the wave source. The method essentially amounts to specifying the covariability between the vorticity forcing and the vorticity, where the vorticity is related to the forcing by the linearized barotropic vorticity equation. The initial motivation for our method came from experiments designed to test the ideas of Chen et al. (2007): changes in wave phase speeds are responsible for

*Corresponding author address: David J. Lorenz, Center for Climatic Research, University of Wisconsin-Madison, 1225 W. Dayton St., Madison, WI 53706.
E-mail: dlorenz@wisc.edu

the poleward shift of the jet in response to external forcing that acts to make the jet stronger. We found that prescribing changes in the phase speed of the forcing led to unintended increases or decreases in wave amplitude depending on whether the new phase speed is closer to the resonance frequency of the free modes of the barotropic model. This made it impossible to separate the contributions of phase speed and wave amplitude to the latitudinal shift of the jet (Chen et al. (2007) found that increasing the wave amplitude also led to a poleward shift, for example). Another problem with forcing the vorticity equation directly is that there is no good way to specify the space-time structure of the forcing based on diagnostics from a General Circulation Model (GCM) or observations. It is easy to see how a control run of a barotropic model with forcing at high versus low phase speeds will be most sensitive to external forcing at different locations solely due to the choices involving the random forcing. By taking our approach, the RWC model can be compared directly to a GCM or to observations using the convergence of the vertical EP flux (Edmon et al. (1980)) in the upper troposphere as the wave source, and moreover the forcing amplitude is automatically tuned so that resonance is not an issue. DelSole (2001) also specified the magnitude of the wave activity source at each latitude in a linearized barotropic model. The temporal structure of the forcing, however, was assumed to be white noise, so the space-time structure of the wave activity source is not necessarily realistic. More importantly, specifying the temporal structure makes it impossible to change the phase speed of the waves independently of changes in the background zonal wind. In our approach, on the other hand, the entire phase speed-latitude-wavenumber structure of the wave activity source is specified and can be manipulated to better understand the dynamics.

In this paper, we develop and test a quantitative model of RWC. In later papers we will use RWC to separate and understand dynamical mechanisms (Lorenz (2014a); Lorenz (2014b)). In sections 2 and 3, we describe the GCM experiments and the implementation of RWC in a linearized barotropic model. Next we compare the RWC simulations with the GCM (section 4). In section 5, we explore the factors that control changes in the phase speed spectrum of the wave activity source and develop a simple quantitative model of the changes in phase speed. In section 6, we couple the RWC model to a simple barotropic model of zonal-mean zonal wind anomalies and show how the coupled RWC model repro-

duces the response of the GCM to reduced friction and the evolution of the GCM's internally generated variability. We end with a brief summary.

2. GCM experiments and diagnostics

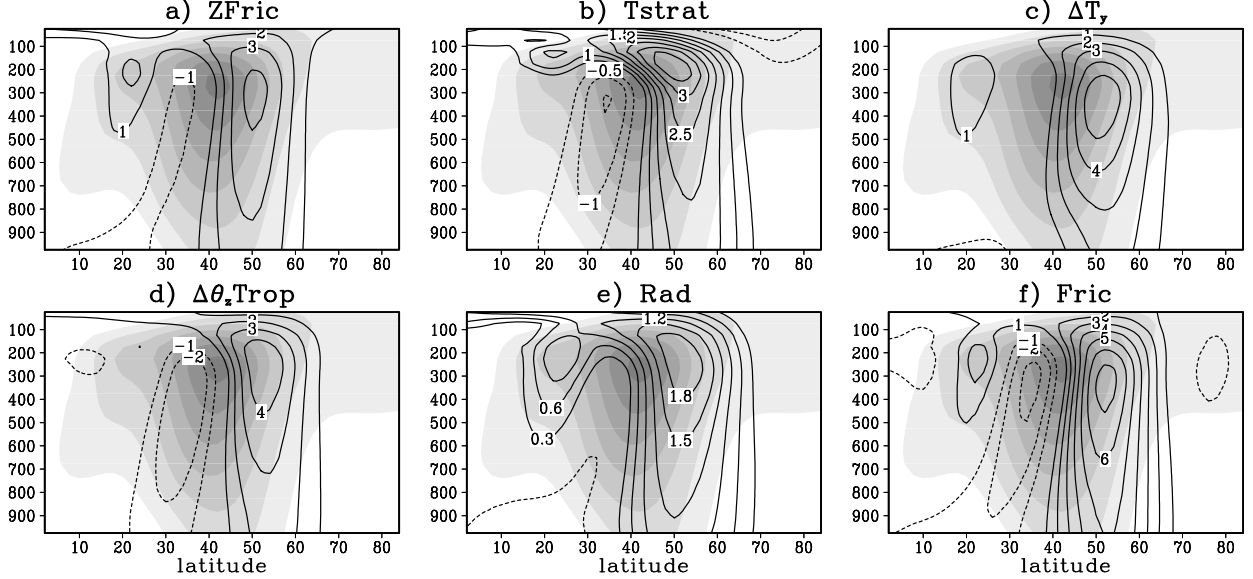
The GCM used in this series of papers is the grid point model described by Held and Suarez (1994). The horizontal resolution is 2.5×2 degrees in longitude and latitude, with 20 equally spaced sigma levels in the vertical. The model uses an Arakawa C-Grid and an explicit leapfrog scheme with a 4.8-minute time step. Details of the dynamical core are described in Suarez and Takacs (1995). All model experiments were run for 4500 days from an isothermal initial condition. Only the final 4000 days were used for analysis. The instantaneous zonal and meridional winds (u , v), potential temperature (θ) and surface pressure (p_s) were archived every 8 hours for analysis. Because the boundary conditions and dynamics are symmetric about the equator, we average the results of both hemispheres together to decrease sampling noise.

The standard idealized forcing given in Held and Suarez (1994) is used as the control run. To understand the response to external forcing we perturb the parameters of the control run in six ways. Following Robinson (1997) and Chen et al. (2007), we decrease the near-surface Rayleigh friction but only the component acting on the zonal-mean u , since this isolates the essential processes important for the poleward shift. We also run a separate integration with friction reduced everywhere. Following Haigh et al. (2005), Williams (2006) and Lorenz and DeWeaver (2007), we increase the tropopause height by decreasing the thermal equilibrium temperature of the stratosphere. Following Gerber and Vallis (2007), we increase 1) the pole-to-equator temperature difference of the thermal equilibrium profile and 2) the rate of relaxation to thermal equilibrium by reducing the thermal relaxation timescale everywhere by a prescribed factor. Finally, we increase the tropical static stability parameter in Held and Suarez (1994). The details of the six experiments and the acronyms used to reference the individual experiments are given in Table 1.

All of the above perturbations have the direct effect of increasing the strength of the jet and therefore, consistent with Kidston and Vallis (2012), they also shift the jet poleward (Fig. 1). The experiments with more poleward shift per degree of strengthening have larger

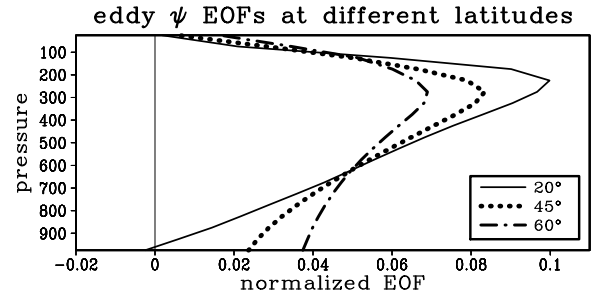
Table 1: Perturbed GCM experiments.

Name	Description	Control Value	Perturbed Value
ZFRIC	decrease friction on zonal mean u	$k_f = 1 \text{ day}^{-1}$	$k_f = 0.8 \text{ day}^{-1}$ on zonal mean u
TSTRAT	decrease stratosphere temp.	$T_{strat} = 200 \text{ K}$	$T_{strat} = 195 \text{ K}$
ΔT_y	increase pole-to-equator temp. diff.	$\Delta T_y = 60 \text{ K}$	$\Delta T_y = 70 \text{ K}$
$\Delta \theta_z \text{TROP}$	increase tropical static stability	$\Delta \theta_z = 10 \text{ K}$	$\Delta \theta_z = 13 \text{ K}$
RAD	decrease thermal relaxation time scale	$k_a = 1/40 \text{ day}^{-1}$ and $k_s = 1/4 \text{ day}^{-1}$	$k_a = 1/35 \text{ day}^{-1}$ and $k_s = 1/3.5 \text{ day}^{-1}$
FRIC	decrease friction	$k_f = 1 \text{ day}^{-1}$	$k_f = 0.8 \text{ day}^{-1}$


 Figure 1: The climatological zonal-mean zonal wind in the control run (shaded) and the change in zonal-mean zonal wind for the six experiments in Table 1 (contours) (m s^{-1}). The x -axis is latitude (degrees) and the y -axis is pressure (hPa).

negative anomalies on the equatorward flank of the time-mean jet (shaded) relative to the positive anomalies on the poleward side. Experiments in this class include TSTRAT, $\Delta \theta_z \text{TROP}$, FRIC and possibly ZFRIC. For a given amount of strengthening, ΔT_y and RAD have a relatively small amount of poleward shift. We will explore how well RWC simulates the eddy momentum fluxes associated with these runs below.

To apply a barotropic model of the eddies to diagnose the multi-level GCM, we must prescribe a single level background zonal wind and absolute vorticity field. To this end, we calculate the vertical Empirical Orthogonal Functions (EOFs) of the eddy ψ over longitude and time for each latitude. The values of the first ψ EOF define the relative weights for averaging the multi-level zonal-mean zonal wind (\bar{u}) and $\beta^* (= a^{-1} \partial_\phi (f + \bar{\zeta}))$ where ϕ is the latitude) into a single number for each latitude. Note that longitude and time are treated the same in the calculation


 Figure 2: The eddy ψ EOFs at three different latitudes. The x -axis is the normalized amplitude and the y -axis is pressure (hPa).

of the EOFs. The leading ψ EOFs peak at the tropopause and their structure is more barotropic at high latitudes than at low latitudes (Fig. 2). Weighting by the vertical ψ profile of the waves is motivated by the calculation of the “equivalent barotropic level” for external Rossby waves in Held et al. (1985) (see their equation 2.10). We calcu-

late the multi-level β^* first and then we apply the vertical weighting. Unless explicitly stated otherwise, this same vertical weighting is applied to all GCM diagnostics that involve a single vertical level of \bar{u} .

Space-time cross-spectral analyses of eddy fluxes are calculated using the method of Randel and Held (1991) except that phase speed spectra are given in terms of angular phase speed (c_ω) instead of phase speed. The temporal spectral analysis is performed over 64 day chunks (= 192 times given the 8 hour sampling time) that overlap by 32 days. The resulting frequency spectrum is further smoothed with a running mean over five adjacent frequency bands. Typically, the stationary phase speed/frequency is not considered because the effects of strong stationary wave sources dominate the observed phase speed spectra. In our GCM with axisymmetric boundary conditions, however, the stationary frequency (phase speed) is not enhanced relative to adjacent frequency bands and we therefore consider the full phase speed spectrum.

For all figures in this paper, angular phase speed is given in terms of velocity at 45° latitude in m s^{-1} . In other words, our angular phase speed (c) is related to the angular phase speed in rad s^{-1} (c_ω) by $c = c_\omega a \cos(45^\circ)$, where a is the radius of the earth. The resolution in phase speed for all analysis and figures is 2 m s^{-1} .

3. Implementing Rossby wave chromatography

The starting point for our implementation of RWC, is the barotropic vorticity equation on a sphere linearized about a background zonal-mean zonal wind, \bar{u} , and absolute vorticity gradient, β^* ($= a^{-1} \partial_\phi (f + \bar{\zeta})$),

$$\frac{\partial \zeta'}{\partial t} + \frac{\bar{u}}{a \cos \phi} \frac{\partial \zeta'}{\partial \lambda} + \beta^* v' - \nu \nabla^2 \zeta' = F', \quad (1)$$

where ζ' , v' and F' are the eddy relative vorticity, meridional velocity and vorticity forcing, ϕ is the latitude, λ is the longitude, a is the radius of the earth, ν is the diffusion coefficient. If the eddy variables are written in the form

$$\eta' = \eta(\phi) \exp(im(\lambda - c_\omega t)), \quad (2)$$

where the unprimed η is a complex amplitude that depends only on ϕ , m is the *integer* zonal wavenumber, and c_ω is the angular velocity, then

$$im \left(\frac{\bar{u}}{a \cos \phi} - c_\omega \right) \zeta + \beta^* v - \nu \nabla^2 \zeta = F, \quad (3)$$

where of course it is straightforward to write the complex v and $\nabla^2 \zeta$ in terms of the complex ζ if desired. The wave activity equation can be found by taking the complex conjugate of (3), multiplying by $\cos \phi \zeta / (2\beta^*)$ and taking the real part

$$\frac{\cos \phi}{2} \Re(\zeta v^*) - \frac{\nu \cos \phi}{2\beta^*} \Re(\zeta \nabla^2 \zeta^*) = \frac{\cos \phi}{2\beta^*} \Re(\zeta F^*). \quad (4)$$

We multiplied by one half above for convenience because the zonal mean of two waves with complex amplitude η and ξ is $\Re(\eta \xi^*)/2$. The first term on the left is the divergence of the wave activity flux ($= -\cos \phi \Re(uv^*)/2$), the second term is the wave activity sink/source from diffusion and the term on the right is the wave activity source, which we want to prescribe. This source term is set equal to the convergence of the vertical component of the wave activity flux

$$\frac{\cos \phi}{2\beta^*} \Re(\zeta F^*) = -\frac{\partial}{\partial p} \left(\frac{f \cos \phi}{2} \frac{\Re(\theta v^*)}{\partial_p \bar{\theta}} \right). \quad (5)$$

In this paper, the analysis is performed as a layer average from σ_t ($= 0.125$) to σ_b ($= 0.525$), so (5) becomes, after transforming to σ ($= p/p_s$) coordinates and rearranging,

$$\Re(\zeta F^*) = \frac{\beta^*}{\sigma_b - \sigma_t} \left(\left[f \frac{\Re(\theta v^*)}{\partial_\sigma \bar{\theta}} \right]_{\sigma_t} - \left[f \frac{\Re(\theta v^*)}{\partial_\sigma \bar{\theta}} \right]_{\sigma_b} \right) \equiv S. \quad (6)$$

Note we have defined the new (real) variable S to be the right hand side of (6). We choose a σ_t in the stratosphere so that there is no significant export of wave activity out of the top of the slab—instead the source is dominated by a positive contribution from tropospheric baroclinic waves. We choose a mid-tropospheric rather than lower-tropospheric level for σ_b because the eddy momentum fluxes are primarily in the upper troposphere. A lower tropospheric level, on the other hand, may not necessarily capture any attenuation of the wave activity flux that may occur as the waves travel upwards. The correspondence between the RWC simulations and the GCM are not very sensitive to the precise values of σ_t and σ_b .

Specifying the source of wave activity amounts to specifying the covariance between ζ and F . Discretizing (6) and writing in component form with a latitude index, j , and writing (3) as a matrix equation in ζ and F as $\zeta_j = \sum_k A_{jk} F_k$, we need to solve

$$\begin{aligned} S_j &= \Re(\zeta_j F_j^*) \\ &= \Re \left(\sum_k A_{jk} F_k F_j^* \right) \end{aligned} \quad (7)$$

where we do *not* follow the repeated index summing convention and all indices run from 1 to n , the number of latitudes. Equation (7) is under-constrained because F_j are complex. One can solve (7) if one provides additional constraints, for example, one can specify that all F_j are real. Equation (7) assumes that the forcing (F_j) is coherent at all latitudes (i.e. the forcing at high latitudes always has the same phase and amplitude relationship to forcing at low latitudes). This assumption works satisfactorily for many m and c_ω , but the solution is subject to noise in F_j at some m and c_ω . Therefore, we assume that we have a large number, T , of possibly independent “realizations” of the forcing, F_{jt} , where t is an index over the realizations. The individual realizations are analogous to the partitioning of data into separate chunks when doing cross spectral analysis. For each realization, we assume

$$\zeta_{jt} = \sum_k A_{jk} F_{kt}.$$

The total “flux” that we need to set equal to S is the average over all realizations

$$\begin{aligned} S_j &= \frac{1}{T} \Re \left(\sum_{kt} A_{jk} F_{kt} F_{jt}^* \right) \\ &= \Re \left(\sum_k A_{jk} \frac{1}{T} \sum_t F_{kt} F_{jt}^* \right) \\ &= \Re \left(\sum_k A_{jk} C_{kj} \right), \end{aligned} \quad (8)$$

where C_{kj} is a complex covariance matrix. We close the problem by specifying the correlation structure \hat{C}_{kj} so that S only determines the amplitude, g_j^2 , of the diagonal elements of C_{kj} :

$$S_j = \Re \left(\sum_k A_{jk} \hat{C}_{kj} g_j g_k \right). \quad (9)$$

Equation (9) is the same form as (7), the only difference is that A_{jk} is multiplied term by term by the correlation matrix. We assume that \hat{C}_{kj} is real (on average, there is no net phase difference between forcing at different latitudes) and of the form:

$$\hat{C}_{jk} = \exp \left(- \left(\frac{\phi_j - \phi_k}{b} \right)^2 \right), \quad (10)$$

where b is a constant. When \hat{C} is real, only the real part of A_{jk} matters for the calculation of g :

$$S_j = \sum_k \Re(A_{jk}) \hat{C}_{kj} g_j g_k. \quad (11)$$

Equation (11) is a system of quadratic equations for the forcing amplitude, g , as a function of latitude that has 2^n complex solutions, where n is the latitude. Almost all solutions are highly oscillatory in latitude and we find that by simply choosing a smooth and broad initial guess we can converge to the relevant smooth g . The details can be found in Appendix A.

S is dominated by positive values. At some values of c_ω , ϕ and m , however, S is slightly negative. We find that for some of these c_ω and m with negative S , there is no real solution to (11) even for general \hat{C}_{kj} (i.e. \hat{C}_{kj} is not necessarily of the form in (10) but is only constrained to be a valid (i.e. positive semi-definite) correlation matrix). If we only take the nonnegative values of S , however, then there is a real solution for all situations that we have encountered. Therefore, the system we solve is:

$$\max(S_j, 0) = \sum_k \Re(A_{jk}) \hat{C}_{kj} g_j g_k. \quad (12)$$

For more details see Appendix A. Note, because S is dominated by positive values, there is “nearly” a valid solution to (11)—the integrated wave activity source in the RWC model is indistinguishable by eye to the GCM wave activity source. Nevertheless, we choose to solve the system (12) with an “exact” solution. Also the constraint of nonnegative S does not necessarily mean that the convergence of vertical EP flux in the upper-troposphere is nonnegative. Instead it means that the convergence of vertical EP flux is the same sign as β^* . In practice, this distinction is only essential at the grid point near the pole in the coupled experiments described below.

Once g is found the momentum flux ($= [u'v']_j$), for example, is

$$[u'v']_j = \frac{1}{2} \Re \left(\sum_{kl} U_{jk} V_{jl}^* \hat{C}_{kl} g_k g_l \right), \quad (13)$$

where U_{jk} and V_{jk} are matrices that relate the forcing, F_k , to the zonal and meridional wind, respectively. All other fluxes can be calculated in a similar way. The above method gives the solution for a particular wavenumber, m , and angular velocity, c_ω . The total solution is simply the sum of the fluxes over all m and c_ω .

The RWC model is applied to the full sphere. In all cases, the background flow that forces the model is symmetric, therefore we only show the results in the Northern Hemisphere. The matrix A_{jk} and the calculation of

u from the stream-function, ψ , are all approximated using simple, centered second-order finite differences on the same grid as the GCM. The boundary conditions are $\psi = 0$ and $\zeta = 0$ at the poles. There are two free parameters: the diffusivity, ν , and the latitudinal scale in the correlation matrix, b . The same ν and b were used for all included wavenumbers, m , and angular phase speeds, c_ω . Only m up to 20 are considered. The model was fit by trial-and-error by simply sweeping through parameter space and using the parameters that gave the smallest error for the momentum flux after integrating over m and c_ω for the control run. The values of ν and b are $6.11 \times 10^5 \text{ m}^2 \text{ s}^{-1}$ and 11.1 degrees, respectively. The same values were used for all experiments here and in Lorenz (2014a) and Lorenz (2014b). The conclusions regarding mechanisms in Lorenz (2014a) and Lorenz (2014b) do not depend significantly on the size of these parameters, which mostly determine the amplitude of the fluxes. For example, both $b = 0$ (no coherence) and $b = \infty$ (perfect coherence) lead to the same conclusions regarding mechanisms.

The value of the diffusion in the RWC model is much larger than the values typically used in a linearized barotropic model. For example, the diffusivity in Held and Phillips (1987) is $1.0 \times 10^3 \text{ m}^2 \text{ s}^{-1}$, which is 611 times smaller than our value. Our diffusivity is large because it is not attempting to model the sub-grid scale diffusion in the GCM, instead it is parameterizing the nonlinear eddy-eddy interactions (i.e. wave breaking) in the GCM. Despite modeling nonlinearities with a simple constant diffusivity, we will see that the RWC model reproduces the main features of the GCM's variability and its response to external forcing. This suggests that the details of the breaking morphology (i.e. anticyclonic versus cyclonic, Thorncroft et al. (1993), Rivière (2011)) are not of first order importance in causing either the structure of the internal variability or the response to external forcing. Instead, our results suggest that any changes in the breaking morphology are determined by the changes in the background flow and not the other way round (Barnes and Hartmann (2012)).

4. Application of Rossby wave chromatography to GCM

In this section, we look at the performance of RWC in simulating the momentum fluxes, $\overline{u'v'}$, given the background zonal-mean flow (\bar{u} and $\beta^* = a^{-1} \partial_\phi (f + \bar{\zeta})$) and

the space-time structure of the wave activity source (= convergence of the vertical component of EP flux (Edmon et al. (1980))). Next, we look at the ability of RWC to simulate the changes in $\overline{u'v'}$ in response to external forcing given the changes in background flow and in the wave activity source. The interpretation of the changes seen here is reserved for later papers. For all comparisons, the GCM momentum fluxes are averaged from $\sigma = 0.125$ to $\sigma = 0.525$ exactly like the convergence of the vertical component of EP flux used to force the RWC model.

As mentioned above, the momentum fluxes integrated over all wavenumbers, m , and angular phase speeds, c_ω were used to tune the two parameters of RWC (Fig. 3a). The largest errors are poleward of 50° where the RWC $\overline{u'v'}$ is greater than the GCM. In addition the main positive center of $\overline{u'v'}$ is shifted slightly poleward in the RWC model. The latitude/phase speed spectrum (Randel and Held (1991)) of the wave activity source, which is specified in RWC, peaks on the equatorward flank of the jet but decays much more quickly to zero on the equator side than on the pole side of the jet (Fig. 3b). The latitude/phase speed spectrum of $\overline{u'v'}$ in the GCM shows that poleward (equatorward) momentum (wave activity) fluxes dominate—this is a fundamental asymmetry caused by the spherical geometry. The momentum fluxes are weighted more toward lower phase speeds compared to the wave source. The RWC $\overline{u'v'}$ reproduces the general features in the GCM $\overline{u'v'}$ but the distribution in latitude and phase speed tends to be less broad than the GCM (Figs. 3de). In particular, the waves in the RWC model do not propagate as far toward the critical level (gray line) compared to the GCM.¹ Poleward of 45° , on the other hand, the bias in the RWC phase speed spectra might be best described as too much propagation: both equatorward by the slower waves (positive $\overline{u'v'}$) and poleward by the faster waves (negative $\overline{u'v'}$). The fact that the former are overestimated more leads to the biases poleward of 50° in Fig. 3a.

The change in the total integrated $\overline{u'v'}$ for each of the six GCM experiments is compared with RWC in Fig. 4. RWC correctly simulates the variability in general structure (monopole versus weak dipole) and the variability in amplitude among the six experiments. In general, the RWC model simulation is too narrow and the nodal line is

¹Note that the linear RWC model has non-zero momentum flux equatorward of the subtropical critical level. This is due to the strong diffusion in the linear barotropic model (see section 3).

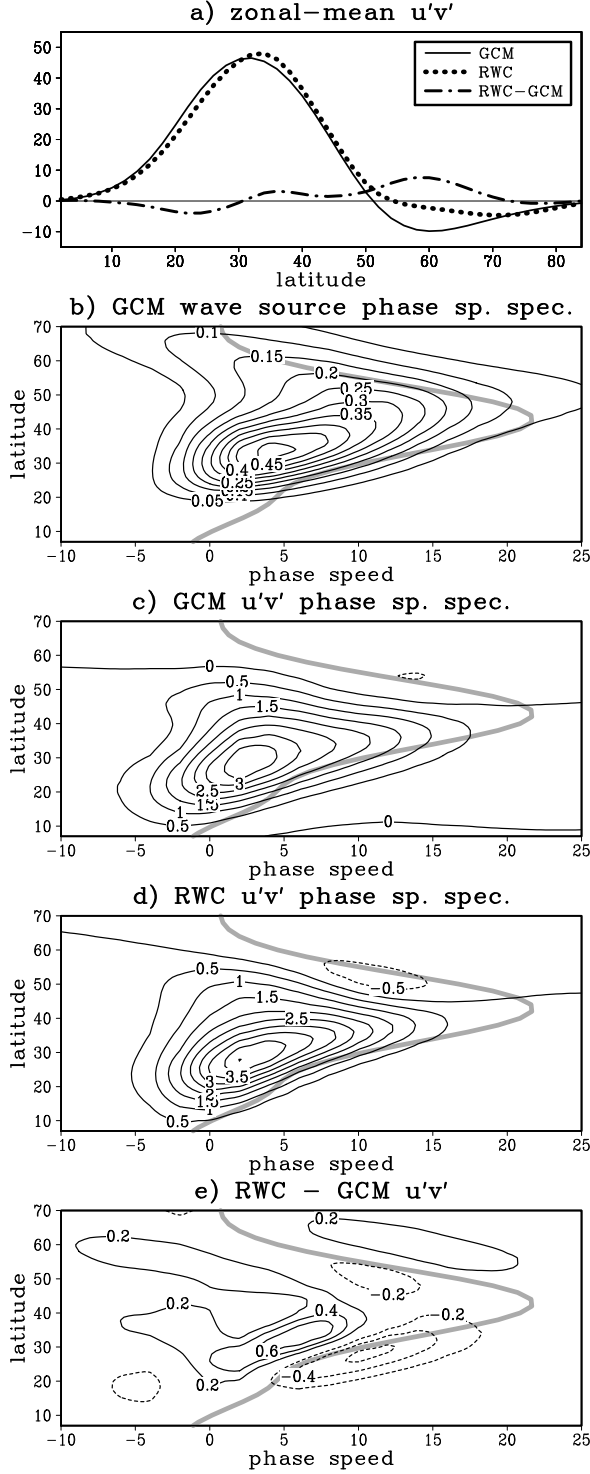


Figure 3: a) RWC eddy momentum flux (dotted), zonal-mean eddy momentum flux averaged from $\sigma = 0.125$ to 0.525 in the GCM (solid) and their difference ($\text{m}^2 \text{s}^{-2}$). b) Latitude/phase speed spectrum of the vertical component of EP flux averaged from $\sigma = 0.125$ to 0.525 in the GCM (day^{-1}). The gray line is the critical level. The x -axis is angular phase speed in m s^{-1} at 45° (see section 2). c) Latitude/phase speed spectrum of the eddy momentum flux averaged from $\sigma = 0.125$ to 0.525 in the GCM (m s^{-1}). d) Latitude/phase speed spectrum of the eddy momentum flux from RWC (m s^{-1}). e) Difference of panels (d) and (c).

too far poleward when the $\overline{u'v'}$ changes are of the dipole type. Interestingly, when the RWC model is coupled to \bar{u} these biases are reduced (4a) (see section 6). The RWC model also tends to under-estimate the magnitude of the $\overline{u'v'}$ changes.

The change in the latitude/phase speed spectrum of $\overline{u'v'}$ for each of the six GCM is compared with RWC in Fig. 5. The most obvious change is an increase in $\overline{u'v'}$ across the jet axis. In some experiments there are significant negative $\overline{u'v'}$ changes and these tend to occur at lower phase speeds than the positive changes. In general, RWC gets all the features of the full GCM and one would have no problem matching the correct RWC simulation with the corresponding GCM if the figures were randomly scrambled. The RWC model has a negative bias just poleward of the critical level on the poleward flank of the jet. This feature is also present in the GCM but its amplitude is below the contour interval. Like the control run latitude/phase speed spectrum, the changes in the RWC spectra tend to be too sharp in latitude and phase compared to the GCM.

While there are clearly significant biases in the RWC model, the RWC simulation reproduces all the general features of the GCM. This suggests that the mechanisms operating in the RWC model are likely the same mechanisms operating in the GCM. Similarly, the mechanisms that do not operate in the RWC probably do not operate in a significant way in the GCM.

5. Change in wave source phase speeds

Below we couple the RWC model to \bar{u} . Because the wave activity source can potentially change with the background flow, we need to be able to model the changes in wave activity source given the background flow. In this section, we propose a very simple model of the changes in wave activity source phase-speed spectra in response to changes in \bar{u} . We consider only the phase speed changes in this paper because the focus is on the simpler case of nearly barotropic anomalies. Based on the results below, we believe that to first order the dynamics related to mechanical forcing and the internal variability can be described without considering changes in wave activity source magnitude. In future work, we will couple the RWC model to the zonal-mean circulation in the latitude-pressure plane and consider the effects of changes in source magnitude.

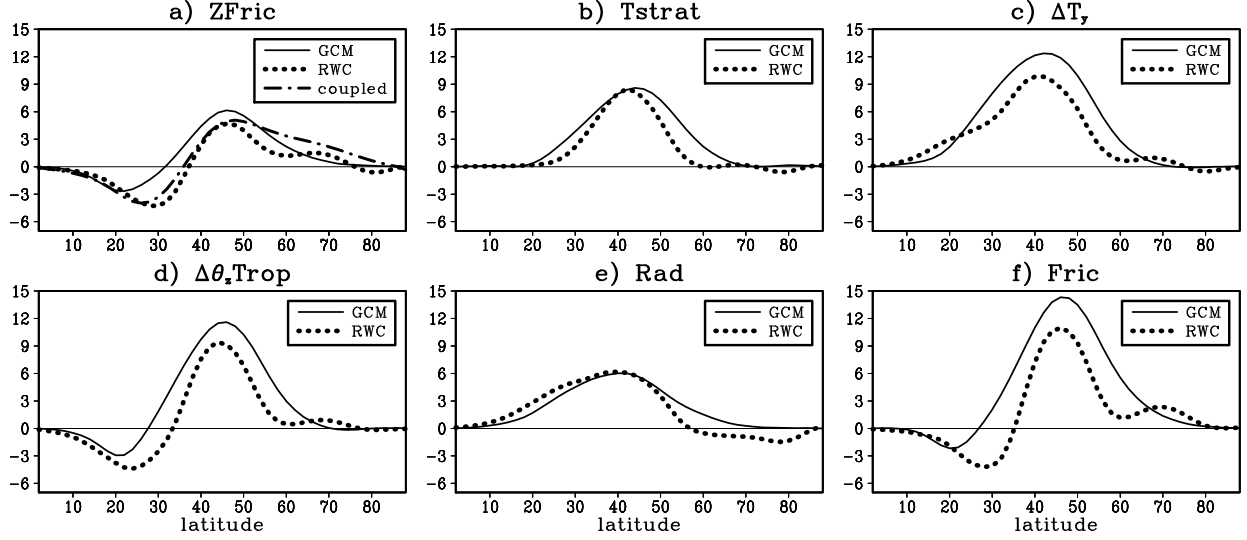


Figure 4: a) The change in zonal-mean eddy momentum flux for ZFRIC in the GCM (solid), RWC (dotted), and for RWC coupled to \bar{u} ($\text{m}^2 \text{s}^{-2}$). b) The change in zonal-mean eddy momentum flux for TSTRAT in the GCM (solid) and RWC (dotted) ($\text{m}^2 \text{s}^{-2}$). c) As in (b) but for ΔT_y . d) As in (b) but for $\Delta \theta_z \text{TROP}$. e) As in (b) but for RAD. f) As in (b) but for FRIC.

a. Diagnosing GCM

First, we want to come to a general understanding of the changes in the phase speed of the wave activity source in the GCM. The inviscid, unforced version of (3) leads to the following dispersion relation:

$$c_\omega = \frac{\bar{u}}{a \cos \phi} - \frac{\beta^* a \cos \phi}{m^2 + l^2}, \quad (14)$$

where l is the meridional wave number. While the changes in \bar{u} and β^* can be estimated directly from the zonal-mean flow the changes in $m^2 + l^2$ can not. In this paper we estimate the total wavenumber squared in the GCM using

$$m^2 + l^2 = \sqrt{\frac{\widehat{\zeta'^2}}{\widehat{\psi'^2}}}, \quad (15)$$

where ζ' and ψ' are the eddy relative vorticity and streamfunction, and the caret denotes averaging in longitude and weighting in the vertical by the scheme in Section 2.

The percent change in $m^2 + l^2$ and β^* for the GCM runs ZFRIC and ΔT_y is shown in Fig. 6a. The GCM run ΔT_y was chosen because it has the biggest scale changes. The changes in β^* dominate over the changes in scale, and moreover the change in scale for ZFRIC is nearly zero. The changes in scale are small enough that (14) can be linearized about the control run and the contribution of the individual terms evaluated. Fig. 6b shows the decomposition for the ΔT_y run. The advection term dominates

the phase speed changes and the β^* term dominates over the scale term.

So far we have estimated the changes in wave phase speed based on the dispersion relation but we have not looked directly at the actual changes in phase speed. To quantify the actual phase speed change in the GCM, we use linear regression to relate the change in wave source to the derivative of the mean wave source:

$$\Delta S = a_0 + a_1 \left(-\frac{\partial S}{\partial c} \right), \quad (16)$$

where a_0 and a_1 are constants. For infinitesimal perturbations, a_1 is the shift of the spectrum in phase speed² and this is plotted for zonal wavenumbers 6, 7 and 8 in Fig. 6c. The actual phase speed changes are about the same magnitude as the phase speeds estimated from the background flow, but the actual phase speed change has a broader distribution in latitude particularly on the equatorward flank (Fig 6c, for ZFRIC). These results suggest that (14) could be used in a parameterization of the effect of \bar{u} on phase speeds and that a more quantitatively accurate model might involve smoothing the background flow and/or the predicted phase speed changes in latitude.

²For example, consider a small shift, δ , in the S profile: $S(c - \delta)$. By a Taylor series: $S(c - \delta) - S(c) \approx -\delta dS/dc$. Therefore the change in S for small shifts is proportional to $-dS/dc$.

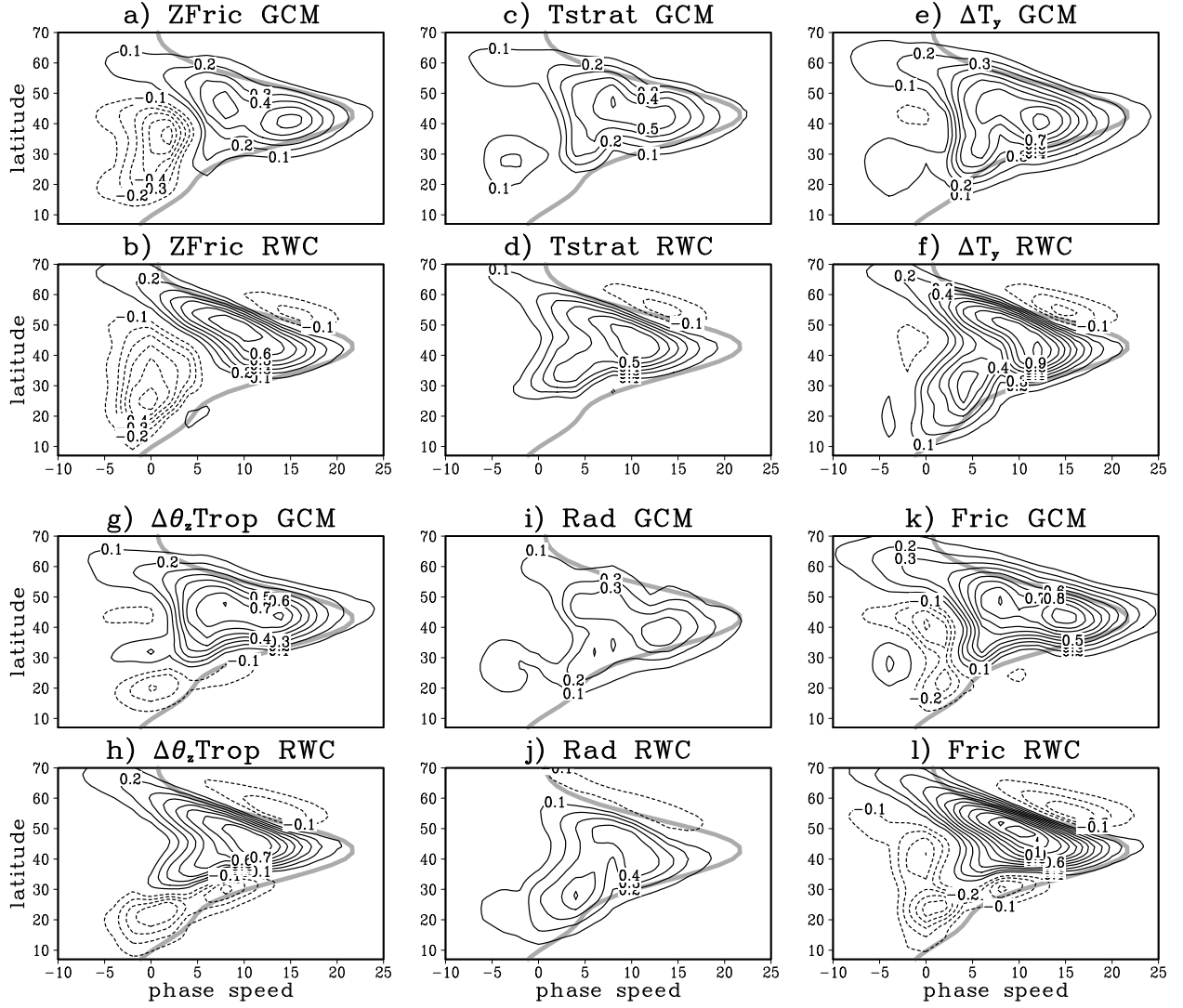


Figure 5: a) The change in the latitude/phase speed spectrum of eddy momentum flux in the GCM for ZFRIC (m s^{-1}). The gray line is the critical level. The x -axis is angular phase speed in m s^{-1} at 45° (see section 2). b) as in (a) but for RWC. c) as in (a) but for TSTRAT. d) as in (b) but for TSTRAT. e) as in (a) but for ΔT_y . f) as in (b) but for ΔT_y . g) as in (a) but for $\Delta \theta_z \text{TROP}$. h) as in (b) but for $\Delta \theta_z \text{TROP}$. i) as in (a) but for RED. j) as in (b) but for RAD. k) as in (a) but for FRIC. l) as in (b) but for FRIC.

b. Simple model of phase speed changes

We now describe a simple model of the phase speed changes based on the dispersion relation (14). We found above that changes in the horizontal wavenumber are small, therefore we assume that $m^2 + l^2$ is constant, so that the phase speed in a perturbed state (subscript 2) can be related to that in the control (subscript 1) by:

$$c_{\omega 2} = \frac{\bar{u}_2}{a \cos \phi} + \frac{\beta_2^*}{\beta_1^*} \left(c_{\omega 1} - \frac{\bar{u}_1}{a \cos \phi} \right). \quad (17)$$

We found above that the actual wave source phase speed changes appear to be smoothed in latitude relative to pre-

dictions based on the dispersion relation. Therefore, for our simple model of the phase speed change, we smooth \bar{u}_1 , \bar{u}_2 , β_1^* and β_2^* with a Gaussian kernel, $\exp(-\phi^2/a_c^2)$, where a_c is 17° latitude, and then we apply (17). The predicted phase speed change is then used to shift the phase speed spectrum of the control run in a conservative way by mapping the power in each phase speed bin to the two bins closest to the new predicted phase speed. To compare the simple model to the GCM, we remove the component of the GCM's change involving changes in source magnitude by rescaling the perturbed wave activity source so that the sum over phase speed is the same as

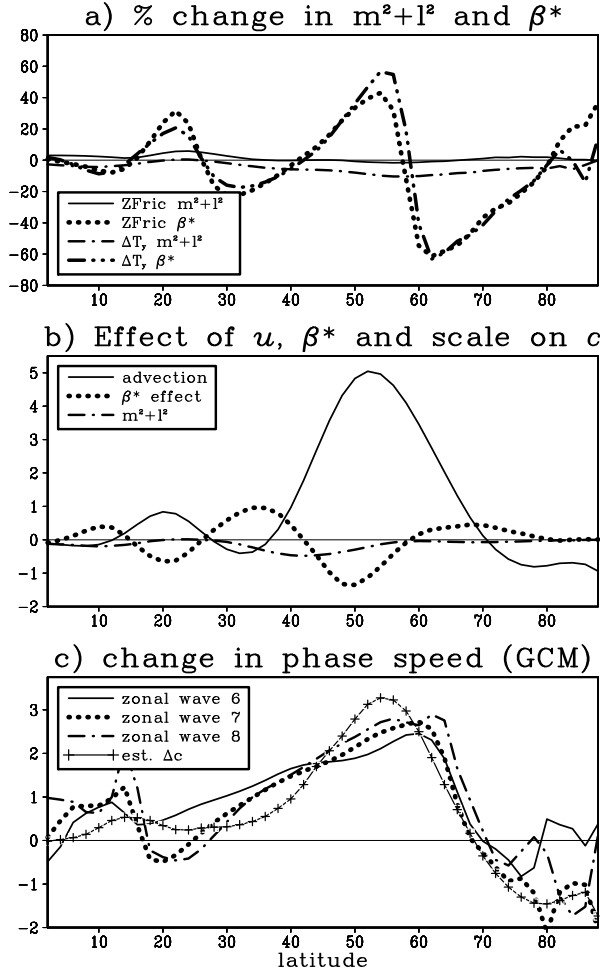


Figure 6: a) The percent change relative to the control for $m^2 + l^2$ in ZFRIC (thin solid), β^* in ZFRIC (thick dotted), $m^2 + l^2$ in ΔT_y (thin dash-dotted) and β^* in ΔT_y (thick dash-dotted). b) Estimate of the effect changes in \bar{u} (thin solid), β^* (thick dotted) and $m^2 + l^2$ (dash-dotted) on the change in wave activity source phase speeds for the run ΔT_y (m s^{-1}). c) Empirical change in phase speed in the GCM for the ZRIC run for zonal wavenumbers 6 (thin solid), 7 (thick dotted) and 8 (dash-dotted). The estimate from the dispersion relation is given by the solid line with plus signs (m s^{-1}).

the control for each ϕ and m . The difference in wave activity source phase-speed spectrum between the rescaled perturbed run minus the control is shown for the reduced zonal-mean friction run (Fig. 7a) and the increased pole-to-equator temperature gradient run (Fig. 7c). The simple model does a reasonable job predicting the magnitude and structure of the phase speed changes (Fig. 7b and Fig. 7d). The largest differences are on the poleward flank of the jet. As expected from Fig. 6b, the advection component dominates and very similar results are obtained by taking $\beta_2/\beta_1 = 1$ in (17) (not shown).

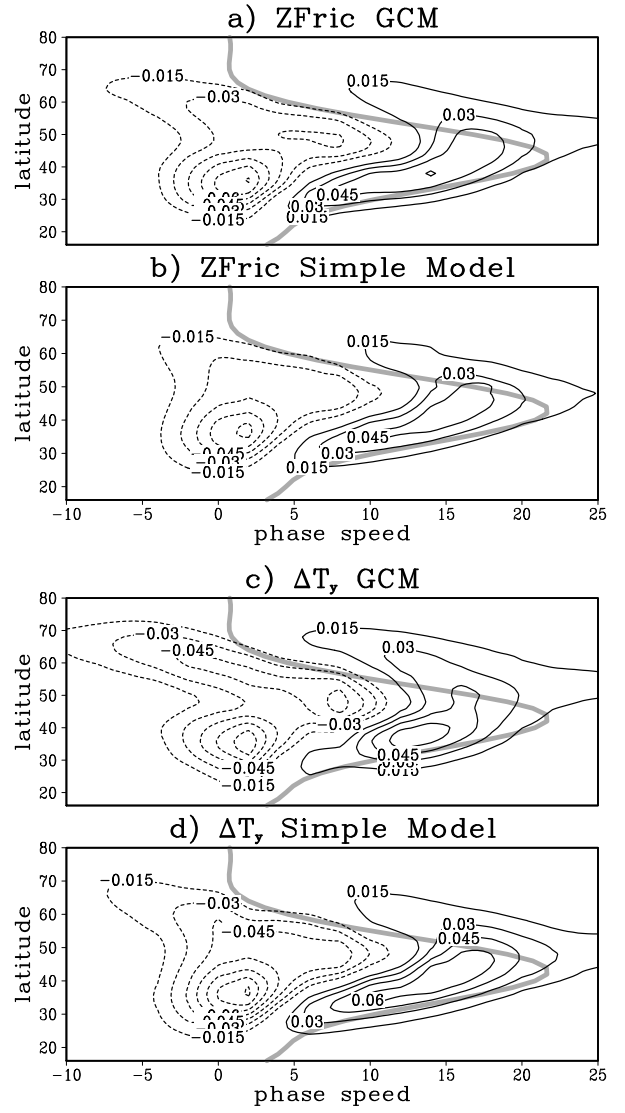


Figure 7: a) The change in the phase speed spectrum of the wave activity source due to changes in phase speed (see text) for the run ZFRIC. Units are day^{-1} . The gray line is the critical level. The x -axis is angular phase speed in m s^{-1} at 45° (see section 2). b) Same as (a) but for the simple model. c) Same as (a) but for the run ΔT_y . d) Same as (b) but for the run ΔT_y .

One unsatisfactory aspect of this simple model is the arbitrary smoothing parameter, a_c . While this smoothing parameter impacts the phase speed changes seen in Fig. 7, we will see that, due to the integrating nature of phase speed changes, this smoothing parameter has amazingly little impact on the momentum fluxes when we use these predicted wave sources to force the RWC model (Lorenz (2014b)).

6. Coupling the RWC model to the Zonal Wind

a. Response to reduced friction

In this section, we describe how the RWC model is coupled to \bar{u} in a way that is consistent with the GCM. We also compare the evolution and equilibrium response of the coupled RWC to the GCM. In this paper, RWC is coupled to a one layer version of \bar{u} :

$$\frac{dz}{dt} = \alpha h - \frac{z}{\tau} + F_z, \quad (18)$$

where z is the modelled one-layer \bar{u} anomaly, h is the eddy vorticity flux anomaly in the RWC model when z is added to the climatological background wind, α and τ are constants that need to be determined and F_z is the external forcing. Following Lorenz and Hartmann (2001), we estimate the parameters α and τ through a cross spectral analysis of the analogs of z and h in the GCM. Unlike Lorenz and Hartmann (2001), who consider vertical averages, the z is the \bar{u} weighted as described in section 2 and h is the eddy vorticity flux averaged from $\sigma = 0.125$ to $\sigma = 0.525$. While vertical averaging makes more sense from the perspective of the momentum budget, the RWC model involves \bar{u} and $\overline{u'v'}$ that are weighted as above. In practice, the budget represented by (18) is nearly as closed as before: the cross spectral coherence drops by only 0.01 when we follow the RWC weighting. The constants α and τ , however, do change with the weighting (α is nearly one in Lorenz and Hartmann (2001)). For the control run, $\alpha = 0.59$ and $\tau = 9.07$ days (see Appendix B). α is less than one because the vertically averaged momentum flux is smaller than the momentum flux averaged over the upper-troposphere.

We now design a coupled RWC experiment that is analogous to the ZFRIC GCM experiment. To determine the correct forcing, F_z , we first calculate the vertically averaged \bar{u} weighted by the Rayleigh friction coefficient in the GCM. We call this zonal wind profile that “feels” the surface friction \bar{u}_F . Reducing the zonal-mean component of friction by 20% is analogous to a forcing that gives rise to a wind anomaly of $0.2\bar{u}_F$ averaged over the Rayleigh friction layer. Therefore, if the wind anomalies are barotropic, then $F_z = \bar{u}_F/\tau$. The anomalies are not quite barotropic, however. Instead the typical ratio of the RWC weighted \bar{u} to the vertically averaged \bar{u} is 1.14 (see Appendix B). Therefore, $F_z = 1.14\bar{u}_F/\tau$. For this particular integration we also want to use a different value for τ : $\tau_2 = 10.68$ days. This value is calculated from the

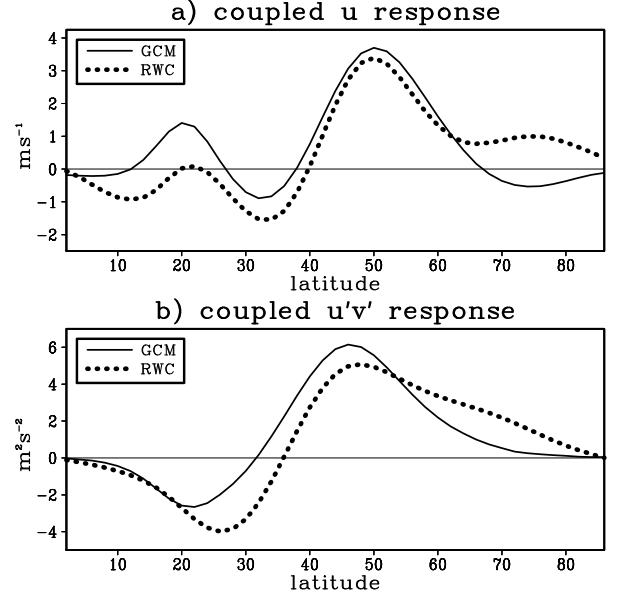


Figure 8: a) The change in \bar{u} in response to reduced zonal-mean component of friction (ZFRIC) in the GCM (thin solid) and the coupled RWC model (thick dotted) (m s^{-1}). b) The change in $\overline{u'v'}$ in response to reduced zonal-mean component of friction (ZFRIC) in the GCM (thin solid) and the coupled RWC model (thick dotted) ($\text{m}^2 \text{s}^{-2}$).

ZFRIC run and is only used in (18) not in the determination of F_z . Note that $\tau_2 < \tau/0.8$, presumably because \bar{u} anomalies are more barotropic in the ZFRIC GCM run.

The coupled model is integrated for 200 days from the initial condition $z = 0$. We found that by smoothing $\overline{\zeta'v'}_{RWC}$ in latitude, we could take a significantly larger time step (= 8 hours) without numerical instability but with negligible impact on the simulation. Therefore we apply a simple 1-2-1 smoothing filter to $\overline{\zeta'v'} \cos^2 \phi$ before forcing z . The smoother operates on $\overline{\zeta'v'} \cos^2 \phi$ instead of $\overline{\zeta'v'}$ because then it is easy to satisfy the constraint that $\overline{\zeta'v'} \cos^2 \phi$ must integrate to zero over ϕ .

The response of the coupled RWC model is quite similar to the GCM response to a 20% reduction in the zonal-mean component of friction (Figs. 8ab). RWC tends to decrease (increase) \bar{u} too much on the equatorward (poleward) side of 50° . For $\overline{u'v'}$, RWC exhibits a poleward shift of the response relative to the GCM and it exaggerates the amplitude of the $\overline{u'v'}$ decreases in the subtropics relative to the $\overline{u'v'}$ increases in the mid-latitudes.

In Fig. 9, we show the anomalies in \bar{u} and $\overline{u'v'}$ for the spin-up of the RWC model to reduced friction conditions. The zonal wind initially becomes stronger over the first few days and then begins shifting poleward almost imme-

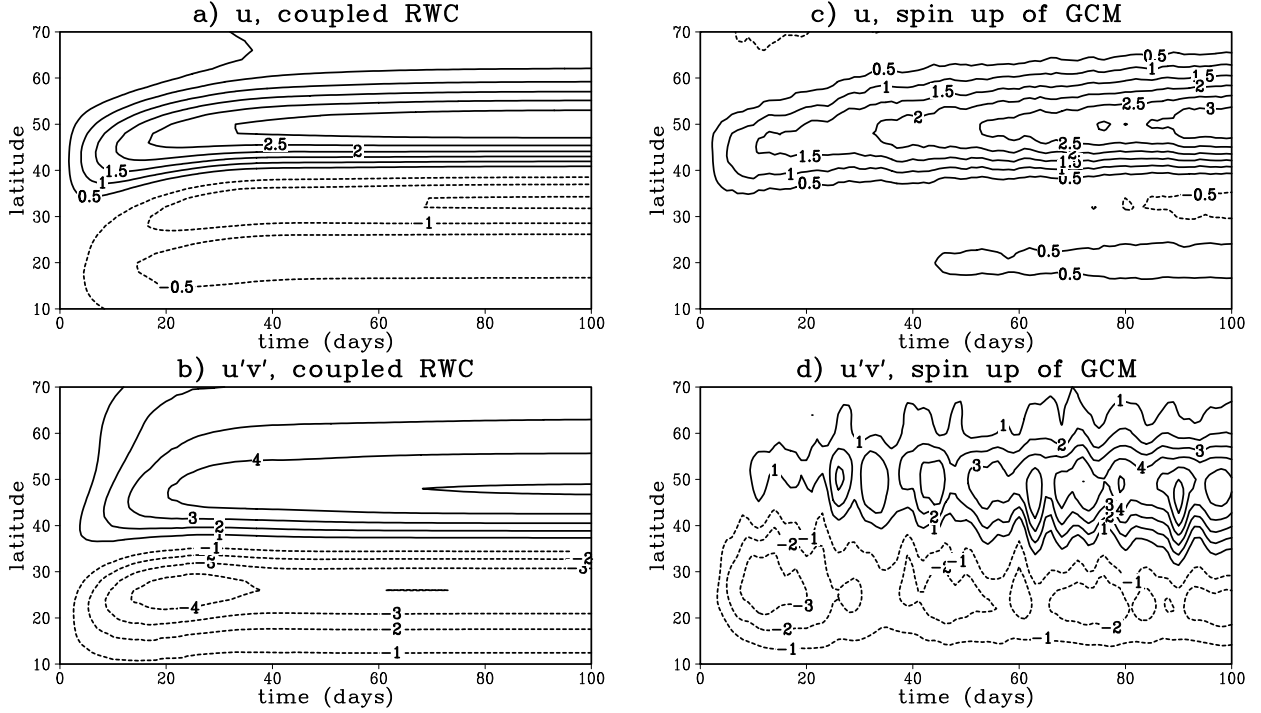


Figure 9: a) Spin-up of \bar{u} anomalies in the coupled RWC model response to instantaneously reduced zonal-mean component of friction (ZFRIC) (m s^{-1}). b) Same as (a) but for $\overline{u'v'}$ ($\text{m}^2 \text{s}^{-2}$). c) Same as (a) but for an average over 1600 spin-ups of the GCM. d) Same as (c) but for $\overline{u'v'}$.

diately (Fig. 9a). The adjustment of \bar{u} to its eventual amplitude, however, takes place on a longer time scale. The presence of at least two time scales is more evident in the momentum flux (Fig. 9b). For example, the reductions in $\overline{u'v'}$ in the subtropics occur quickly over the first 15 days and then actually weaken slightly afterwards. The $\overline{u'v'}$ increases on the poleward flank of the jet, on the other hand, gradually equilibrate over the entire 100 day time period. This time scale contrast is also evident in the “average” spin-up of the GCM to an instantaneous reduction in the zonal-mean component of friction. Here the “average” GCM spin-up is an average of 800 100-day integrations with initial conditions taken in 5 day increments from the control run. We also average the results from the southern and northern hemispheres together to increase the number of effective spin-up samples. The presence of two GCM time scales is most evident in the $\overline{u'v'}$ evolution although the long time scale is longer in the GCM and the short time scale is shorter in the GCM (Fig. 9d). Comparison of the GCM and RWC \bar{u} evolution is hampered by the negative \bar{u} bias in the subtropics of the coupled RWC model. The fact that the RWC model reproduces the presence of the two time scales implies that the explanation does not involve 1) the dynam-

ics of the zonal-mean meridional circulation in the latitude/pressure plane, 2) multiple time scales of adjustment to different diabatic processes or 3) differing time scales among different eddy processes. Instead, the different time scales represent different amplitudes and/or sign of the eddy momentum flux feedback for the z “modes” of the system. For example, suppose the RWC model is linearized: $h = Bz$, where B is a matrix. Let λ_j be the eigenvalues of the matrix B , then the time scales for the adjustment of the different eigenvectors or “modes” is $(1/\tau - \alpha\lambda_j)^{-1}$. The larger the positive feedback, λ_j , the larger the time scale. The presence of the two time scales is consistent with the fact that EOF1 of \bar{u} is associated with a positive eddy feedback while EOF2 is not (Lorenz and Hartmann (2001)). In Lorenz (2014b) we will explore the mechanisms behind the selective eddy reinforcement of various \bar{u} anomalies.

The difference in time-scales implies that the magnitude of the eddy feedbacks are biased in the RWC. For EOF1 anomalies, the de-correlation time in the RWC is 22 days compared to 35 days in the GCM. This bias could be due to a baroclinic feedback³ or it could be simply

³By baroclinic feedback, we mean that 1) the latitudinal profile of the wave activity source (integrated over phase) changes significantly

a result of biases in our implementation of RWC: RWC tends to underestimate the response even when it is given the full change in the wave activity source spectrum (Fig. 4). Another source of bias might be the fact that the eddies respond instantaneously to changes in the background \bar{u} in our implementation of RWC.

b. Internal variability

In this section, we confirm that the coupled RWC model can reproduce aspects of the internal variability of the GCM. Lorenz and Hartmann (2001) and Lorenz and Hartmann (2003) argue that the variability in the eddy momentum flux can be usefully partitioned into a random component and a component that is proportional to the \bar{u} anomaly. To avoid the complications of characterizing the random component of $\overline{u'v'}$, we only consider the evolution of \bar{u} after the \bar{u} anomalies have been set up. To this end, we perform a one-point lag regression analysis on the GCM \bar{u} anomalies (e.g. Feldstein (1998)). The one-point lag regression of pentad \bar{u} anomalies on the \bar{u} anomaly at 22° is shown in Fig. 10a. The positive lags shown represent the typical future evolution of \bar{u} following anomalies at 22° . After one pentad the amplitude of the lag 0 pattern has weakened considerably. After that point the anomalies slowly migrate poleward as in Feldstein (1998). Switching to a base point of 34° , we still see the rapid decay after one pentad but the anomalies remain stationary afterwards instead of propagating poleward.

To simulate this evolution in the coupled RWC model, (18) is integrated as an initial value problem with $F_z = 0$. The initial conditions are the \bar{u} anomalies at lag 0 in Figs. 10ab. The RWC model does a good job simulating the poleward propagation versus the persistence of the anomalies associated with the base points 22° (Fig. 10c) and 34° (Fig. 10d). However, the RWC model does not simulate the rapid transient decrease in amplitude seen in the GCM (see below). In addition, it fails to capture the degree of asymmetry in the high versus low latitude \bar{u} responses, particularly for the 22° basepoint.

It turns out that the rapid transient decay is due to a transient negative eddy feedback. To see this consider a large number of initial value problems taken from a control run of the GCM but with the zonal-mean state

in response to the \bar{u} anomalies and that 2) this change in wave source is responsible for the resulting momentum flux anomalies. In these results there is no baroclinic feedback because the latitudinal profile of the wave activity source is constant.

modified to be like either the positive or negative phase of EOF1. After averaging over 1460 initial value problems and both hemispheres and taking the difference between the positive and negative phase of EOF1 we get Fig. 11 (This is a standard Held and Suarez (1994) run but with the horizontal resolution half that of all other experiments shown here). The vertically averaged \bar{u} anomaly decays rapidly over the first few days and then afterwards is maintained at a relatively constant amplitude. The vertically averaged $\overline{u'v'}$ anomaly initially acts to damp the \bar{u} anomalies and then reverses sign and maintains the anomalies. Watterson (2002) found similar behavior in a barotropic model initialized with EOF1-type anomalies. Looking at the momentum budget in more detail it is clear that $\overline{u'v'}$ “explains” the behavior of the \bar{u} anomalies (not shown). This transient effect is not a result of nonlinearities in the response of $\overline{u'v'}$ to \bar{u} amplitude as experiments with half amplitude EOF1 anomalies demonstrate (not shown). Instead we believe this is a transient negative response to any changes in \bar{u} . The EOF1 example shown is the most dramatic case because the eddy forcing reverses in time. The dynamics of this transient negative feedback is the subject of future work. Note that this negative feedback is evident in the lag correlations in, for example, Lorenz and Hartmann (2001) and Lorenz and Hartmann (2003), but they attributed this negative effect to the random burst of momentum flux immediately proceeding the peak \bar{u} anomaly rather than to background \bar{u} itself.

Since the RWC model is a steady state model, we do not expect it to capture the above transient negative feedback. However, it appears that the transient feedback has a similar effect on all \bar{u} anomalies so we can simply scale the RWC model \bar{u} anomalies to account for the transient negative feedback. First, we need to quantify the degree of amplitude change and poleward shift. Let $u(\phi_j, t)$ be the latitudinal profile of the \bar{u} anomalies at lag t and latitude grid points ϕ_j for a particular base point. The relative amplitude ($= A$) and latitudinal shift ($= \phi_0$) at lag t relative to lag 0 are the values of A and ϕ_0 that minimize

$$\sum_j (u(\phi, t) - Au(\phi - \phi_0, 0))^2. \quad (19)$$

We minimize (19) using the Levenberg-Marquardt algorithm under the assumption that linear interpolation holds between grid points and that $u(\phi - \phi_0, 0) = 0$ when $\phi - \phi_0$ is outside of the domain. The relative amplitude and latitude shift of the GCM pattern at lag 2 pen-

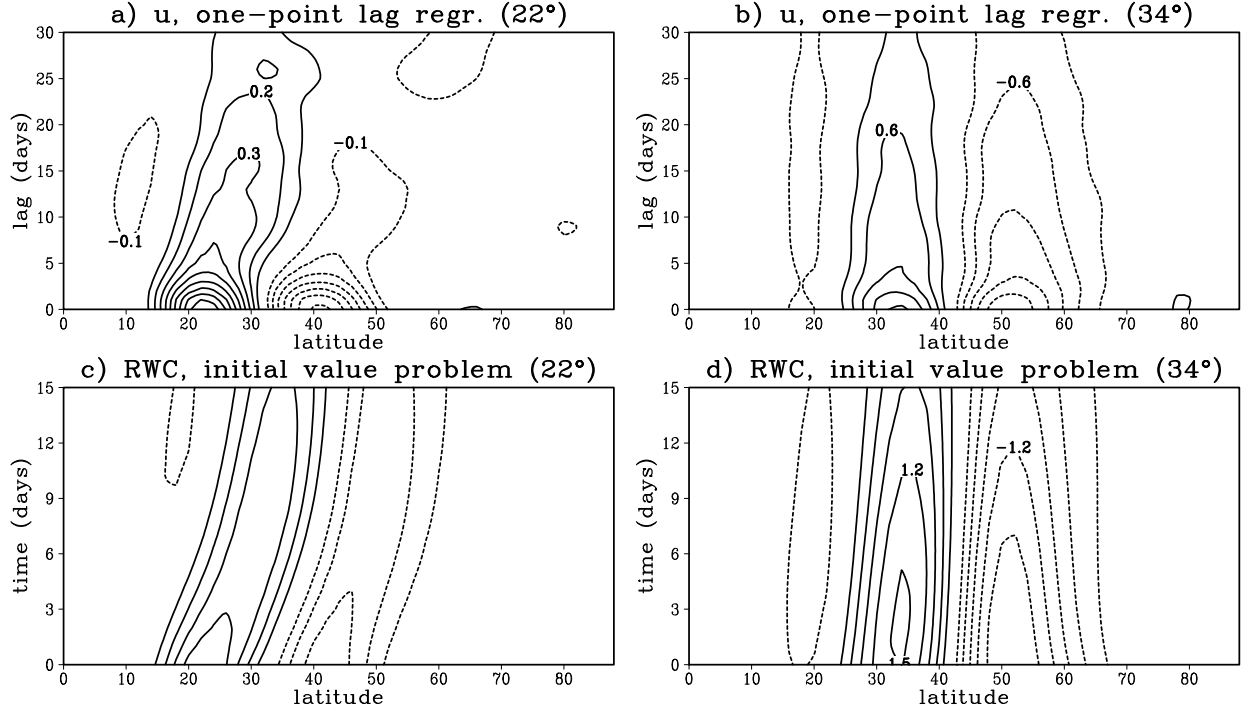


Figure 10: a) One point lag regression of \bar{u} at each latitude with \bar{u} at 22° . Positive lags mean that \bar{u} at 22° leads (m s^{-1}). b) One point lag regression of \bar{u} at each latitude with \bar{u} at 34° . c) Evolution of \bar{u} anomalies taken from lag 0 in (a) as simulated by the coupled RWC model. d) Evolution of \bar{u} anomalies taken from lag 0 in (b) as simulated by the coupled RWC model.

tads relative to lag 0 for all base points is shown in Fig. 12. The amplitude is most persistent for base points nearly in phase with the two dominant centers of action of EOF1 (32° and 52° , not shown). The amplitude peak is relatively flat because the EOF1 structure dominates the one-point regressions of all base points close to 32° and 52° . There are relative minima at the latitude of the time-mean jet (42°) and at two locations in the subtropics. The rate of propagation in latitude varies quite sharply in latitude with a sawtooth-type pattern (Fig. 12b). At points equatorward (poleward) of the poleward center of action of EOF1 (52°), \bar{u} anomalies tend to propagate poleward (equatorward) although there are some exceptions. Most notably, anomalies just poleward of the equatorward center of action of EOF1 tend to propagate “back” equatorward toward this persistent center of action.

We analyze the RWC model in the same way except we compare $t = 0$ to $t = 5$ days because the RWC model evolves faster than the GCM. Also, to take into account the rapid transient decay in the GCM we scale the RWC model amplitude by 0.74. After these modifications, the RWC model does a good job simulating the internal variability of the GCM, particularly for the relative ampli-

tude (Fig. 12). We believe that the RWC model is close enough to the GCM that we can learn useful information about the GCM’s dynamics through the analysis of the RWC model. In future work, we plan to characterize the “random component” of $\overline{u'v'}$ variability and to better understand and characterize the transient negative feedback.

7. Experiments with Prescribed Forcing

In this paper, we take the view that it is much better to prescribe the wave activity source than the vorticity forcing. In this section we give an explicit example of the problems associated with specifying the vorticity forcing by analyzing the response to reductions in the zonal-mean component of friction (ZFRIC). First we show the vorticity forcing from our RWC method as derived from the wave activity source and the background flow (Fig. 13a). Compared to the wave activity source (Fig. 3b), the forcing is much more confined to the center of the mean jet. We now change the phase speed of the forcing using the simple phase speed model in section 5 with the background \bar{u} and β^* from the ZFRIC run (Fig. 13b). Alternatively we could keep the forcing constant, but in this case the results below are even

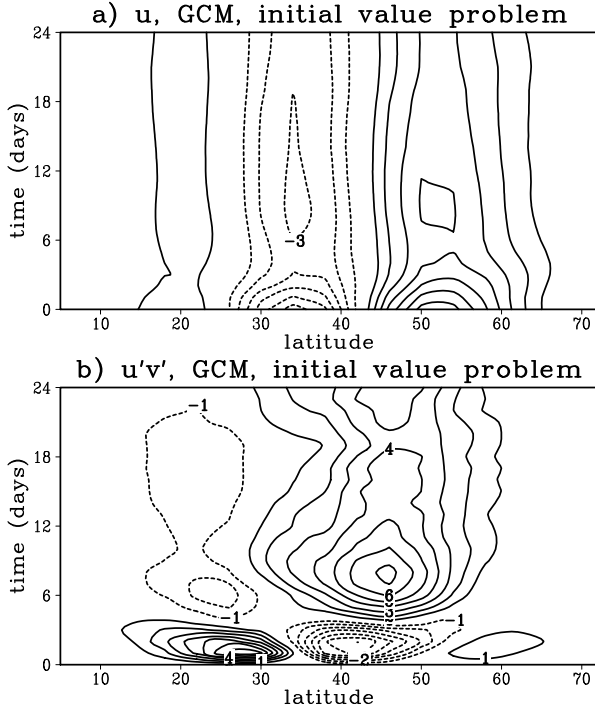


Figure 11: a) Average response of \bar{u} in the GCM to positive EOF1 anomalies in the zonal-mean state minus the average response of \bar{u} to negative EOF1 anomalies in the zonal-mean state (m s^{-1}). The average response is an average over 1460 initial value problems with prescribed zonal-mean state but with eddy fields taken at regular intervals from a long control run. b) Same as (a) but for $\overline{u'v'}$ ($\text{m}^2 \text{s}^{-2}$).

more exaggerated. The forcing anomalies in Fig. 13b are associated with the wave source anomalies in Fig. 13c, which should be compared with the effect of changing phase of source directly (Fig. 7b). The maximum amplitude of the wave source changes when we manipulate the forcing directly (Fig. 13c) are a factor of five larger than the source changes in the GCM and in the simple phase speed model (Figs. 7ab). The effect of the large changes in source associated with prescribed forcing are very evident in momentum flux response from the linearized barotropic model (Fig. 13d). For example, the large increases in momentum flux on both the poleward and equatorward flanks of the jet are a response to similar changes in the wave sources (Fig. 13c). Alternatively, if one instead shifts the phase speeds of the wave source spectrum (Fig. 7b), the momentum flux response looks very much like the full response (compare Fig. 13e to Fig. 5b). One might argue that the results above are impacted by the fact that the phase speed model was tuned to the wave sources and not the vorticity forcing. However it is likely impossible to improve the response to pre-

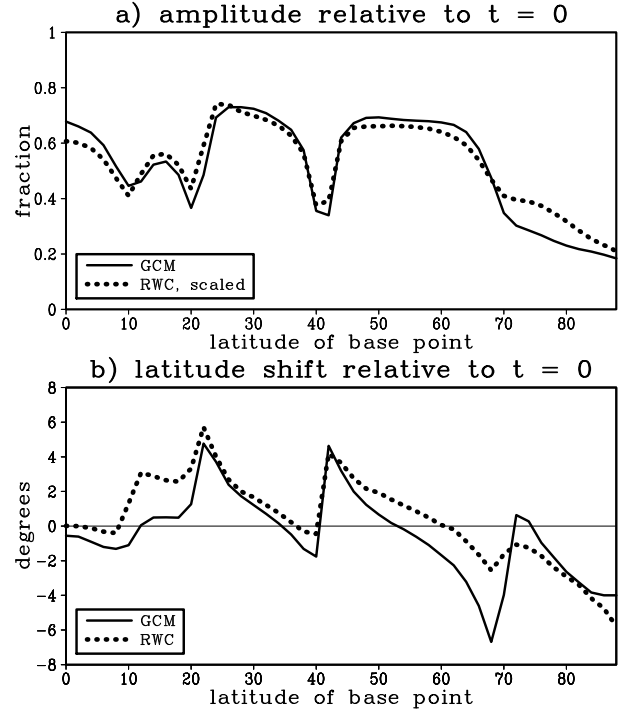


Figure 12: a) Estimate of the change in amplitude at lag 2 pentads relative to the lag 0 one-point regression plot of \bar{u} in the GCM (thin solid). The change in amplitude is shown as a function of the latitude of the base point (x -axis). The change in amplitude for the coupled RWC model at 5 days and scaled by a factor of 0.74 (see text) for initial conditions taken from the lag 0 one-point regression plots of the GCM (thick dotted). b) Estimate of the shift in latitude at lag 2 pentads relative to the lag 0 one-point regression plot of \bar{u} in the GCM (thin solid). The shift in latitude is shown as a function of the latitude of the base point (x -axis). The shift in latitude for the coupled RWC model at 5 days for initial conditions taken from the lag 0 one-point regression plots of the GCM (thick dotted).

scribed forcing unless one takes into account that the amplitude of response to a given forcing depends critically on the proximity to resonance. Even then, the response is likely still inferior to simply prescribing wave source directly as we have done here.

A related forcing approach might be to consider the quasi-geostrophic vorticity equation at upper levels:

$$\frac{\partial \zeta}{\partial t} + \nabla \cdot (\mathbf{v} \zeta) - \nu \nabla^n \zeta = -fD, \quad (20)$$

where D is the divergence and n is the order of the hyper-diffusion in the full model. One can then manipulate the divergence and the background flow separately to understand the dynamics. We have implemented the above scheme in a two level quasi-geostrophic model on a sphere. Unfortunately the scheme gives unrealistic

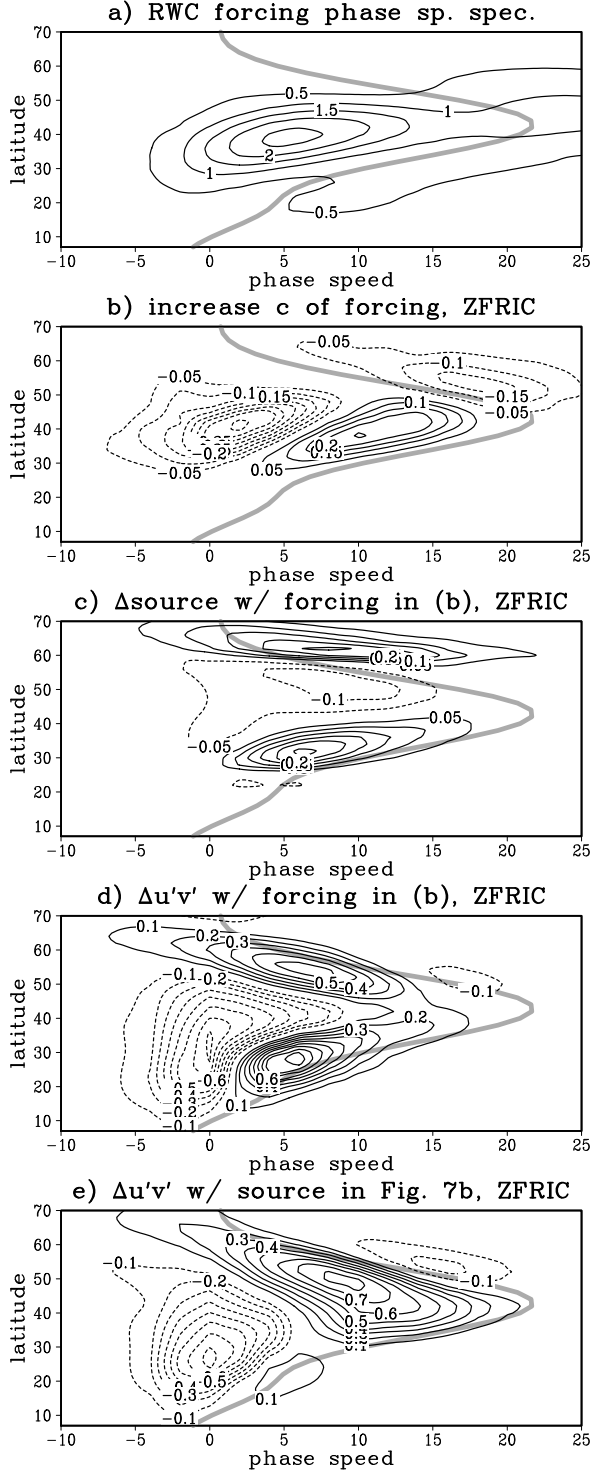


Figure 13: a) Latitude/phase speed spectrum of the vorticity forcing integrated over zonal wavenumber for the control run of RWC. b) The change in the vorticity forcing spectrum (ZFRIC) after changing the phase speeds of the control forcing using the phase speed model. c) The change in the wave activity source spectrum associated with changes in \bar{u} , β^* and the forcing in (b) for the ZFRIC run. d) Same as (c) but for the momentum flux spectrum. e) The change in the eddy momentum flux spectrum associated with changes in \bar{u} , β^* and the wave source changes (rather than the forcing) taken from the phase speed model (i.e. the wave source changes in Fig. 7b).

momentum fluxes because the coupling between the vorticity and divergence in a baroclinic model is missing. This results in an unrealistic wave activity source. Our method works because it is faithful to the wave activity budget, which is the most important constraint given that we are ultimately after the meridional wave activity flux ($= -\overline{u'v'} \cos \phi$).

8. Summary

Rossby Wave Chromatography (RWC) (Held and Phillips (1987)) is implemented in a linearized barotropic model. By RWC, we mean that we calculate the space-time (i.e. phase speed-latitude-wavenumber) structure of the upper tropospheric eddy momentum fluxes given the background zonal-mean flow and the space-time structure of the baroclinic wave activity source (convergence of vertical EP flux (Edmon et al. (1980)) in the upper troposphere). Unlike other studies of the forced barotropic vorticity equation, which specify the vorticity forcing directly (Vallis et al. (2004); Barnes et al. (2010); Barnes and Hartmann (2011); Kidston and Vallis (2012)), we specify the wave source and find the forcing that is consistent with the wave source. The method essentially amounts to specifying the covariability between the vorticity forcing and the vorticity, where the vorticity is related to the forcing by the linearized barotropic vorticity equation. Some advantages of this technique are: 1) the model can be compared directly to a GCM or to observations using the convergence of the vertical EP flux (Edmon et al. (1980)) in the upper troposphere as the wave source, 2) prescribing observed wave activity sources eliminates almost all choices regarding the space-time structure of the forcing, 3) the wave activity source is more closely related to the momentum fluxes (i.e. the meridional wave activity flux) than the vorticity forcing, and 4) the wave activity source and the background flow are decoupled so that one can be changed without impacting the other.

The RWC model reproduces the important features of the mean momentum fluxes of the GCM and the responses of the momentum fluxes to poleward shifted jets in response to changes in friction, pole-to-equator temperature gradient, tropopause height, radiative relaxation time scale or tropical static stability. We also develop a simple model of the changes in the phase speeds of the wave activity sources. This simple phase speed model and the RWC model are coupled to a one-layer version of

\bar{u} anomalies. The coupled model successfully simulates the poleward shift in response to reduced friction and the evolution of GCM's internal variability as diagnosed using one point lag regressions of \bar{u} (Feldstein (1998)). In Lorenz (2014a) and Lorenz (2014b), we will use RWC to understand the dynamical mechanisms responsible for mid-latitude jet variability and change.

Acknowledgments.

The author would like to thank Paulo Ceppi, Jian Lu, Dan Vimont and three anonymous reviewers for their helpful comments and suggestions on the manuscript. This research was supported by NSF grants ATM-0653795 and AGS-1265182.

APPENDIX A

Finding the forcing from the wave activity source

In this Appendix, the procedure for solving (12) is described. Since there are 2^n complex solutions, where n is the number of latitudes, we also describe numerical experiments intended to understand the character of the solutions. It turns out we have a good sense of the structure of all 2^n solutions and the relevant solution is simply the smoothest one with the least zero crossings. Finally, we discuss the proof that there is sometimes no solution unless we take only the non-negative values of S_j , $\max(S_j, 0)$.

a. Algorithm

We solve the system of quadratic equations using 1) a modification to Newton's method involving an exact line search and 2) a simple rescaling operation. The form of the (real) system we need to solve is

$$Q_j = \sum_k B_{jk} g_j g_k - S_j = 0, \quad (\text{A1})$$

where B_{jk} and S_j are given, g_j is to be determined, all indices run from 1 to n and we do *not* follow the repeated index summing convention. Please contact the author for the code that solves this system of quadratic equations (Matlab and Fortran90).

The rescaling operation takes advantage of the fact that if g'_j is a guess of the solution, then it is easy to find the optimal scaling of g'_j that minimizes the error

($= \sum_j Q_j^2$): define S'_j as the wave activity source associated with g'_j :

$$S'_j = \sum_k B_{jk} g'_j g'_k. \quad (\text{A2})$$

Clearly if we scale g'_j by $\sqrt{\alpha}$, then S'_j is scaled by α . With this scaling, the error as a function of α is

$$\sum_j Q_j^2 = \sum_j (\alpha S'_j - S_j)^2, \quad (\text{A3})$$

and this is minimized when

$$\alpha = \frac{\sum_j S_j S'_j}{\sum_j S_j'^2}. \quad (\text{A4})$$

Therefore, the new rescaled guess of the solution, g''_j , is:

$$g''_j = \sqrt{\alpha} g'_j. \quad (\text{A5})$$

We now describe our implementation of Newton's method with exact line search. We first find the Jacobian, J_{jl} , of Q_j :

$$J_{jl} \equiv \frac{\partial Q_j}{\partial g'_l} = B_{jl} g'_j + \delta_{jl} \sum_k B_{lk} g'_k, \quad (\text{A6})$$

where g'_j is a guess of the solution. The Newton's method increment, p_j , is the solution to:

$$\sum_k J_{jk} p_k = -Q_j = S_j - S'_j, \quad (\text{A7})$$

where S'_j is defined by (A2). p_j defines the search direction and we find the λ such that $g'_j + \lambda p_j$ minimizes the error. Substituting $g'_j + \lambda p_j$ in the quadratic system, we have:

$$Q_j = L_j \lambda + N_j \lambda^2 + S'_j - S_j, \quad (\text{A8})$$

where L_j is the linear term ($= \sum_k J_{jk} p_k$)⁴ and N_j is the nonlinear term ($= \sum_k B_{jk} p_j p_k$). Minimizing $\sum_j Q_j^2$ therefore reduces to minimizing a quartic polynomial:

$$a_4 \lambda^4 + a_3 \lambda^3 + a_2 \lambda^2 + a_1 \lambda + a_0, \quad (\text{A9})$$

⁴Note: in this particular case, $L_j = S_j - S'_j$

where

$$\begin{aligned}
a_4 &= \sum_j N_j^2 \\
a_3 &= 2 \sum_j L_j N_j \\
a_2 &= \sum_j (2N_j (S'_j - S_j) + L_j^2) \\
a_1 &= 2 \sum_j L_j (S'_j - S_j) \\
a_0 &= \sum_j (S'_j - S_j)^2. \tag{A10}
\end{aligned}$$

To minimize (A9), we take the derivative and find the roots of the resulting cubic equation using the direct non-iterative algorithm in Press et al. (1992). If there are multiple real roots for the cubic (rare), we pick the root that minimizes (A9). After finding the optimal λ , the new, updated guess of the solution is $g'_j + \lambda p_j$.

We combine the rescaling operation and the Newton's method as follows: given an initial guess, we first rescale the guess. We then repeat the following operations: 1) Newton's method with exact line search, 2) rescaling, and 3) check for convergence. Our convergence criterion is:

$$\left(\frac{\sum_j (S'_j - S_j)^2}{\sum_j S_j^2} \right)^{1/2} < 10^{-7}. \tag{A11}$$

The above algorithm converges almost all the time. For example, all the RWC results in Figures 3 - 8 never failed to converge using the above algorithm. When wind anomalies are in the tropics and/or the polar regions, however, the above algorithm will fail to converge for a few combinations of phase speed and wavenumber (although when integrating over phase speed or wavenumber, the GCM wave source and the RWC wave source are indistinguishable by eye). Therefore, we describe an improved routine below that has converged in all experiments we have performed.

If the above algorithm fails to converge after 20 iterations, we also perform an exact line search in the direction of the gradient of $\sum_j Q_j^2$ (i.e. the steepest descent direction). This steepest direction, q_j , is given by:

$$q_j = - \sum_k J_{kj} (S'_k - S_k). \tag{A12}$$

Note that we multiply $S'_k - S_k$ by the *transpose* of J . Given this alternative search direction q_j , we use (A9) and (A10) to calculate the minimum along this direction, where $L_j = \sum_k J_{jk} q_k$ and $N_j = \sum_k B_{jk} q_j q_k$. We then compare the minimum error ($= \sum_j Q_j^2$) along the Newtonian and steepest descent directions and then use the method with the minimum error to update g'_j .

As mentioned above, the algorithm that implements this entire scheme is available from the author.

b. Initial Condition

If the matrix B_{jk} is diagonal then the equations are uncoupled and the system (A1) is easy to solve:

$$g_j = \pm \sqrt{S_j / B_{jj}}. \tag{A13}$$

Our initial condition for the numerical algorithm is based on (A13) but with a modification to make the algorithm more robust. Let

$$f_j = \sqrt{S_j / b_j}. \tag{A14}$$

Note we take the positive solution of (A13) in (A14) for all cases. The algorithm is more robust if we add a constant positive offset to the initial condition, therefore we choose an the initial g'_j that is:

$$g'_j = f_j + \frac{1}{n} \sum_j f_j. \tag{A15}$$

c. Character of Solutions

In the case of diagonal B_{jk} it is easy to understand the structure of the 2^n solutions. In this case the solutions for each latitude are uncoupled but the sign of the solution is undetermined. Therefore, there are two possible outcomes at each latitude (positive or negative) and n independent latitudes implying there are the 2^n solutions. The individual solutions all have the same absolute value but have different numbers and locations of zero crossings. Similar behavior appears in our more general case when instead of initializing with all $g'_j > 0$ we randomly change the sign of g'_j at some latitudes. An example for $m = 7$ and $c = 8 \text{ m s}^{-1}$ is shown in Fig. 14. With highly oscillatory initial g_j , the algorithm converges to a valid solution with the same phase as the initial g_j . We have confirmed this result by running a large number of tests on all wavenumbers and phase speeds and with different

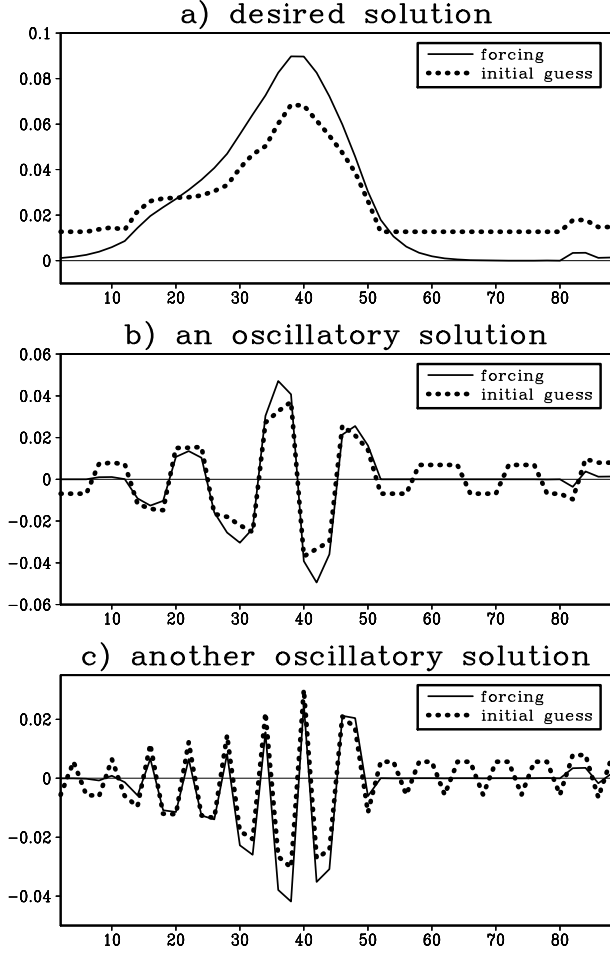


Figure 14: a) The rescaled initial guess for the vorticity forcing of the barotropic model (thick dotted) and the converged solution for the vorticity forcing that provides the correct wave activity source (thin solid). The x -axis is latitude. b) Same as (a) but for a rescaled initial guess with oscillations in sign. The thin solid line also provides the correct wave activity source. c) Same as (b) but for an initial condition that oscillates more rapidly.

frequency oscillations in g_j . When there are significant wave activity sources at a given latitude (the source magnitude is at least 1% of the maximum source for that m and c), the sign of the final g_j is the same as the initial g_j 99.7% of the time. Since the most physical solution is likely the solution with the fewest oscillations, it appears that by initializing with all $g_j > 0$ we are converging toward the most relevant solution in almost all cases (we have confirmed that the RWC simulation of the GCM is worse if we take a meridional wavenumber one solution to (A1)).

d. Non-negativity of the Source

In this subsection, we briefly describe an alternative solution to (8) because it provides a proof of the infeasibility of the wave activity source constraint in some cases. The method also justifies a simple and minor non-negativity constraint on the wave activity source that leads to a valid solution in all cases we have encountered.

The alternate solution for the problem (8) does not assume specific form to the correlation matrix (i.e. (10)). Instead one only assumes that the covariance matrix C is a positive semi-definite matrix (so that it is indeed a realizable covariance matrix) and that it is real (on average, there is no net phase difference between forcing at different latitudes). One can then close the problem by assuming that the correct solution is the solution with the minimum amplitude forcing ($\min \sum_{jt} F_{jt}^2 = \min \sum_j C_{jj}$). Under these conditions there is a single solution that can be found by framing the problem as a “semidefinite programming” optimization problem: we want to minimize:

$$\min \sum_j C_{jj}, \quad (\text{A16})$$

subject to the following constraints:

$$S_j = \sum_k \Re(A_{jk})C_{kj}, \quad (\text{A17})$$

and C_{jk} is positive semidefinite. The final $\overline{u'v'}$ solution to this problem is not much different than the method used in the manuscript (not shown), but it gives slightly inferior results. Therefore we use the original method. A very important result of the semi-definite programming solution, however, is that, for some particular m and c_ω , it proves that the problem given by (A17) has no valid solution that satisfies the constraints (via what is called a “certificate of primal infeasibility”). Note this is a much stronger condition than proving that (A1) has no real solution because no assumptions about the structure of the correlation matrix have been made. It turns out that by simply setting the negative values of S_j to zero, however, there is a valid solution for all cases we have encountered. Since S_j is dominated by positive values, this has very little effect on the integrated S_j .

APPENDIX B

Finding the constants in the one-layer zonal wind equation

In this appendix, we determine the constants α and τ in (18). For this calculation, z is the principal component of the first EOF of the vertically weighted average \bar{u} . The weights for the vertical averaging are described in section 2. The time series h is the vertically averaged eddy vorticity flux anomalies from $\sigma = 0.125$ to $\sigma = 0.525$ projected onto the above EOF. Because we are analyzing the internal variability, $F_z = 0$ in this case.

First, it is most convenient to write (18) in the form:

$$k_1 \frac{dz}{dt} + k_2 z = h, \quad (\text{B1})$$

where k_1 and k_2 are constants. Taking the Fourier spectrum of (B1):

$$(2\pi i k_1 \nu + k_2) Z = H, \quad (\text{B2})$$

where capital letters denote the Fourier transform and ν is the frequency. Multiplying by the complex conjugate of Z and rearranging:

$$2\pi i k_1 \nu + k_2 = \frac{H Z^*}{Z Z^*}. \quad (\text{B3})$$

$H Z^*$ is the cross spectrum and $Z Z^*$ is the power spectrum. The real part of their ratio averaged from $\nu = 0$ to 0.25 days^{-1} defines the constant k_2 . The slope in ν of the imaginary part of their ratio defines $2\pi k_1$ (the least squares slope is fit from $\nu = 0$ to 0.25 days^{-1}). Finally, $\tau = k_1/k_2$ and $\alpha = k_1^{-1}$.

The remaining constant is the ratio (γ) of the RWC weighted \bar{u} ($= z$) to the vertically averaged \bar{u} ($= \bar{z}$), where z and \bar{z} are the first principal components of the corresponding variables. We define γ as the average real part of $Z \bar{Z}^* / \bar{Z} \bar{Z}^*$ from $\nu = 0$ to 0.25 days^{-1} .

REFERENCES

- Barnes, E. A. and D. L. Hartmann, 2011: Rossby wave scales, propagation, and the variability of eddy-driven jets. *J. Atmos. Sci.*, **68**, 2893–2908.
- Barnes, E. A. and D. L. Hartmann, 2012: Detection of Rossby wave breaking and its response to shifts of the midlatitude jet with climate change. *J. Geophys. Res.*, **117**, D09 117.
- Barnes, E. A., D. L. Hartmann, D. M. W. Frierson, and J. Kidston, 2010: Effect of latitude on the persistence of eddy-driven jets. *Geophys. Res. Lett.*, **37**, L11 804.
- Chen, G., I. M. Held, and W. A. Robinson, 2007: Sensitivity of the latitude of the surface westerlies to surface friction. *J. Atmos. Sci.*, **64**, 2899–2915.
- DelSole, T., 2001: A simple model for transient eddy momentum fluxes in the upper troposphere. *J. Atmos. Sci.*, **58** (20), 3019–3035.
- Edmon, H. J., B. J. Hoskins, and M. E. McIntyre, 1980: Eliassen-Palm cross sections for the troposphere. *J. Atmos. Sci.*, **37**, 2600–2616.
- Feldstein, S. B., 1998: An observational study of the intraseasonal poleward propagation of zonal mean flow anomalies. *J. Atmos. Sci.*, **55**, 2516–2529.
- Gerber, E. P. and G. K. Vallis, 2007: Eddy-zonal flow interactions and the persistence of the zonal index. *J. Atmos. Sci.*, **64**, 3296–3311.
- Haigh, J. D., M. Blackburn, and R. Day, 2005: The response of tropospheric circulation to perturbations in lower-stratospheric temperature. *J. Climate*, **18**, 3672–3685.
- Held, I. M. and B. J. Hoskins, 1985: Large-scale eddies and the general circulation of the troposphere. *Advances in Geophysics.*, **28**, 3–31.
- Held, I. M., R. L. Panetta, and R. T. Pierrehumbert, 1985: Stationary external Rossby waves in vertical shear. *J. Atmos. Sci.*, **42** (9), 865–883.
- Held, I. M. and P. Phillips, 1987: Linear and nonlinear barotropic decay on the sphere. *J. Atmos. Sci.*, **44**, 200–207.
- Held, I. M. and M. J. Suarez, 1994: A proposal for the intercomparison of the dynamical cores of atmospheric general circulation models. *Bull. Amer. Meteor. Soc.*, **75**, 1825–1830.
- Kidston, J. and G. K. Vallis, 2012: The relationship between the speed and the latitude of an eddy-driven jet in a stirred barotropic model. *J. Atmos. Sci.*, **69**, 3251–3263.
- Lorenz, D. J., 2014a: Understanding mid-latitude jet variability and change using Rossby wave chromatography: Poleward shifted jets in response to external forcing. *submitted to J. Atmos. Sci.*
- Lorenz, D. J., 2014b: Understanding mid-latitude jet variability and change using Rossby wave chromatography: Wave-mean flow interaction. *submitted to J. Atmos. Sci.*
- Lorenz, D. J. and E. T. DeWeaver, 2007: Tropopause height and zonal wind response to global warming in the IPCC scenario integrations. *J. Geophys. Res.*, **112**, D10 119.
- Lorenz, D. J. and D. L. Hartmann, 2001: Eddy-zonal flow feedback in the Southern Hemisphere. *J. Atmos. Sci.*, **58**, 3312–3327.
- Lorenz, D. J. and D. L. Hartmann, 2003: Eddy-zonal flow feedback in the Northern Hemisphere winter. *J. Climate*, **16**, 1212–1227.
- Press, W. H., B. P. Flannery, S. A. Teukolsky, and W. T. Vetterling, 1992: *Numerical Recipes in Fortran 77: The Art of Scientific Computing*, Vol. 1. Cambridge University Press.
- Randel, W. J. and I. M. Held, 1991: Phase speed spectra of transient eddy fluxes and critical layer absorption. *J. Atmos. Sci.*, **48**, 688–697.
- Rivière, G., 2011: A dynamical interpretation of the poleward shift of the jet streams in global warming scenarios. *J. Atmos. Sci.*, **68**, 1253–1272.
- Robinson, W. A., 1997: Dissipation dependence of the jet latitude. *J. Climate*, **10**, 176–182.
- Suarez, M. J. and L. L. Takacs, 1995: Documentation of the Aries/GEOS dynamical core: Version 2. Tech. Rep. NASA Tech. Memo. 104606, Goddard Space Flight Center, 45 pp., Greenbelt, MD, USA.
- Thorncroft, C. D., B. J. Hoskins, and M. E. McIntyre, 1993: Two paradigms of baroclinic-wave life-cycle behaviour. *Quart. J. Roy. Meteor. Soc.*, **119**, 17–55.
- Vallis, G. K., E. P. Gerber, P. J. Kushner, and B. A. Cash, 2004: A

- mechanism and simple dynamical model of the North Atlantic Oscillation and annular modes. *J. Atmos. Sci.*, **61**, 264–280.
- Watterson, I., 2002: Wave-mean flow feedback and the persistence of simulated zonal flow vacillation. *J. Atmos. Sci.*, **59** (7), 1274–1288.
- Williams, G. P., 2006: Circulation sensitivity to tropopause height. *J. Atmos. Sci.*, **63**, 1954–1961.